Controlling Crystal Polymorphism in Organic-Free Synthesis of Na-Zeolites

Miguel Maldonado,[†,‡] Matthew D. Oleksiak,[†,‡] Sivadinarayana Chinta,[§] and Jeffrey D. Rimer*[,†]

[†]Department of Chemical and Biomolecular Engineering, University of Houston, Houston, Texas 77204, United States
[§]Research and Technology Center, Total Petrochemicals and Refining USA, Inc., La Porte, Texas 77571, United States

S *Supporting Information*

ABSTRACT: Controlling polymorphism is critical in areas such as pharmaceuticals, biomineralization, and catalysis. Notably, the formation of unwanted polymorphs is a ubiquitous problem in zeolite synthesis. In this study, we propose a new platform for controlling polymorphism in organic-free Na-zeolite synthesis that enables crystal composition and properties to be tailored without sacrificing crystal phase purity. Through systematic adjustment of multiple synthesis parameters, we identified ternary (kinetic) phase diagrams at specific compositions (i.e., Si, Al, and NaOH mole fractions) using colloidal silica and sodium aluminate. Our studies identify multiple stages of zeolite phase transformations involving the framework types FAU, LTA, EMT, GIS, SOD, ANA, CAN, and JBW. We report an initial amorphous-to-crystalline transition of core-shell particles (silica core and alumina shell) to low-density framework types and their subsequent transformation to more dense structures with increasing temperature and/or time. We show that reduced water content facilitates the formation of structures such as EMT that are challenging to synthesize in organic-free media and reduces the synthesis temperature required to achieve higher-density framework types. A hypothesis is proposed for the sequence of phase transformations that is consistent with the Ostwald rule of stages, wherein metastable structures dissolve and recrystallize into more thermodynamically stable structures. The ternary diagrams developed here are a broadly applicable platform for rational design that offers an alternative to time- and cost-intensive methods of *ad hoc* parameter selection without *a priori* knowledge of crystal phase behavior.
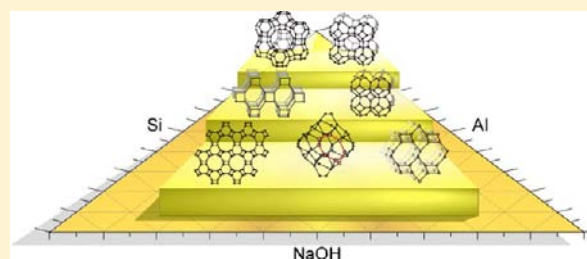
INTRODUCTION

The unique acidity, thermal stability, and shape selectivity of nanoporous zeolites are utilized in industrial applications spanning catalysis to ion exchange. Zeolites are among the most commonly used catalysts in petroleum refining and chemicals production.[1] Significant efforts have been directed toward the optimization of their catalytic activity for additional applications, such as the selective catalytic reduction of nitrogen oxides (NO and NO_2) from emissions[2,3] and biofuels production from renewable resources.[4] Global industries employing zeolites account for approximately $1.9 billion in annual revenue.[5] Many successful methods for enhancing the performance of zeolites for catalysis or selective separations use synthetic routes that employ novel organic structure-directing agents (SDAs) to tailor crystal size and habit;[6–9] however, it is desirable to synthesize zeolites in the absence of organics due to economic considerations, most notably the high manufacturing cost of SDAs, which are irrecoverable due to postsynthesis calcination. One of the critical challenges in organic-free synthesis is preventing the formation of polymorphs (i.e., crystal impurities). To this end, more rational approaches can be developed to optimize zeolite properties while simultaneously providing a flexible design space to adjust synthesis parameters independently without sacrificing crystal phase purity. Typical synthesis parameters include the silicon-to-

aluminum ratio, which affects the acidity and hydrothermal stability of zeolites, and the growth solution pH and water content, which can be adjusted to tailor zeolite size and crystal habit.[10,11] It is not fully understood how many of these parameters impact the kinetics and thermodynamics of zeolite nucleation and crystallization, which is a contributing factor to the frequent formation of crystal polymorphs in zeolite synthesis. To this end, we seek to develop a method for *a priori* control of zeolite polymorphism through the judicious selection of synthesis parameters.

Among the nearly 200 framework types, only a fraction of the known natural and synthetic zeolites crystallize in the absence of a SDA. There have been many studies of zeolite synthesis in organic-free media. Early work by Breck, Flanigen, and others[12,13] examined numerous framework types, such as FAU, LTA, SOD, and CAN (where each zeolite crystal structure is referred to with a 3-letter code assigned by the International Zeolite Association[14]). These studies established a pedagogical approach for analyzing organic-free zeolite synthesis (so-called $Na_2O-SiO_2-Al_2O_3-H_2O$ systems) by describing qualitative trends in crystal phase behavior with ternary phase diagrams constructed from the molar composi-

tions of silicon, aluminum, and extra-framework cation (typically alkali or ammonium ions). This pioneering work was largely empirical, providing general guidelines rather than specific compositions to achieve pure crystal phases. There have been many subsequent studies of organic-free zeolite crystallization at different synthesis conditions that focused on a select number of parameters, such as synthesis time,[15,16] temperature,[17] water content,[18,19] Si and Al sources,[20] solution aging,[21] and extra-framework cations.[22] Collectively, these studies have provided general trends to achieve phase-pure zeolites, but neglect to consider the cumulative effect(s) of multiple parameters, which is necessary to identify and fully utilize the available design space for zeolite synthesis.

Zeolites are thermodynamically metastable relative to more dense structures, such as quartz.[23] As such, zeolite crystallization often involves structural transformations from one metastable structure to more thermodynamically stable structures. This process can be described by the Ostwald rule of stages, which is a ubiquitous phenomenon in natural and synthetic crystallization.[24] One of the most frequently studied zeolite phase transformation is zeolite A (LTA framework) to zeolite X or Y (FAU framework).[12,15,22] Several other phase transformations have been reported, although the vast majority of these involve the use of SDAs to provide kinetic pathways for synthesizing less thermodynamically stable structures and/or the formation of structures that otherwise could not be formed in the absence of the SDA.[25,26] Several groups have examined transformations of zeolite seeds in alkaline solutions whereby seed dissolution and recrystallization into another structure occurred in the absence of SDAs.[27,28] Other groups have performed similar studies of seeded zeolite transformations in the presence of SDAs.[29,30]

Here we present an investigation of six parameters influencing zeolite crystallization: temperature, time, composition (Si, Al, and NaOH mole fractions), and water content. We developed kinetic phase diagrams based on ternary plots of Si−Al−NaOH molar composition. Within these diagrams, we quantitatively identified regions of phase-pure and multiphase zeolite structures. We observed that by systematically varying crystallization time, temperature, and/or water content, we can synthesize numerous crystal structures. This study presents a unique, facile method to characterize zeolite phase behavior through the development of kinetic phase diagrams, which are a new platform for tuning zeolite crystallization. This method identifies a well-defined design space whereby the synthesis parameters can be adjusted to tailor zeolite properties without sacrificing phase purity. Herein, we discuss the synthesis of eight Na-zeolite framework types that form in organic-free media. Moreover, we propose a new hypothesis for zeolite nucleation and offer a rational explanation for the thermodynamic driving force of phase transformations between crystal structures.

■ EXPERIMENTAL SECTION

Zeolite growth solutions were prepared with molar compositions X SiO_2:Y Al_2O_3:11 NaOH:Z H_2O by mixing sodium aluminate (technical grade, Alfa Aesar) and sodium hydroxide (98%, Sigma Aldrich) in deionized water (DI, 18.2 MΩ). These solutions were stirred until well-mixed, and then LUDOX AS-40 colloidal silica (40%, Sigma Aldrich) was added as the silica source. Solutions were stirred for 24 h prior to being placed in a Teflon liner, which was loaded into a stainless steel autoclave and heated in a ThermoFisher Precision oven at temperatures of 65−230 °C. Autoclaves were removed after heating for times that ranged from 1 h to 21 days. Upon removal from

the oven, the autoclave was cooled to ∼25 °C in a water bath for 1 h. The solid crystals were recovered by three cycles of centrifugation and washing with DI water. Centrifugation was performed using a Beckman Coulter Avanti J-E at 5 °C and 13,000 rpm for 45 min. The gel product was dried in air at room temperature overnight prior to analysis.

Kinetic phase diagrams were constructed from zeolite growth solutions at constant 11 NaOH:Z H_2O molar ratios (where Z = 66, 95, 190, or 348). The quantities of silica and alumina used in each synthesis were varied to adjust the silicon-to-aluminum ratio of the growth solution, which we refer to herein as $SAR_{(liq)}$. Experiments in this study were restricted to solutions with molar ratio Si/OH < 1 and a $SAR_{(liq)}$ spanning 0.5 (in the Al-rich region) to 5 (in the Si-rich region). For studies of ANA-type zeolite, we tested synthesis solutions with $SAR_{(liq)}$ as high as 82.

Zeolite crystal structures were determined by powder X-ray diffraction (XRD) using a Siemens D5000 X-ray diffractometer. We label the Bragg peaks on the XRD patterns with symbols for each zeolite framework, as shown in Figure 1 for FAU and LTA. The crystal
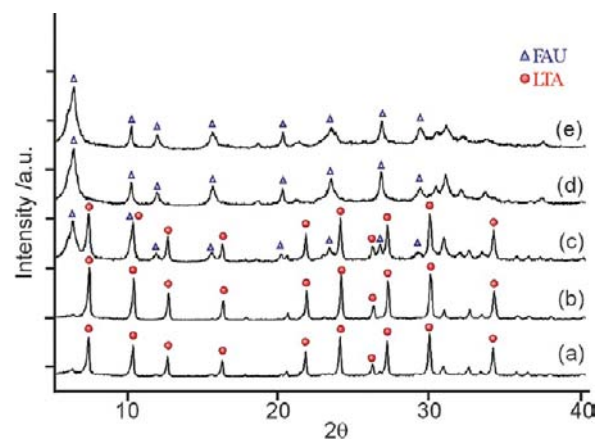

Figure 1. XRD patterns of solids extracted from growth solutions with molar composition 11 NaOH:190 H_2O heated at 65 °C for 7 days. The crystalline products, LTA and/or FAU, were obtained using the following $SAR_{(liq)}$ values: (a) LTA, 0.5; (b) LTA, 1.0; (c) LTA-FAU, 1.25; (d) FAU, 1.5; and (e) FAU, 2.0.

phase(s) were indexed using simulated patterns, which we obtained from the Zeolite Structural Database[14] (reference XRD patterns are provided in Figure S7 of the Supporting Information [SI]). The crystal size and habit were analyzed by electron microscopy using a FEI-235 dual-beam focused ion beam scanning electron microscope (SEM). Details of sample preparation and procedures for SEM, TEM, and dynamic light scattering measurements are provided in the online SI.

■ RESULTS AND DISCUSSION

Kinetic Phase Diagrams. In this section we discuss zeolite crystallization as a function of four synthesis parameters: three compositions (silicon, aluminum, and hydroxide mole fractions) and temperature. The extra-framework cation selected for these studies was Na$^+$, which is commonly used in organic-free synthesis of zeolites. All syntheses employed colloidal silica (LUDOX) as the silica source and sodium aluminate as the aluminum source. We restricted our studies of zeolite crystallization to growth solutions with molar ratios Si/OH < 1 (pH > 13) and focused primarily on syntheses with $SAR_{(liq)}$ ranging from 0.5 to 5, i.e. typical compositions for zeolite syntheses reported in the literature.

Here, we compare zeolite crystallization at different synthesis parameters using ternary diagrams (Figure 2), which plot the mole fractions of silicon, aluminum, and hydroxide used to
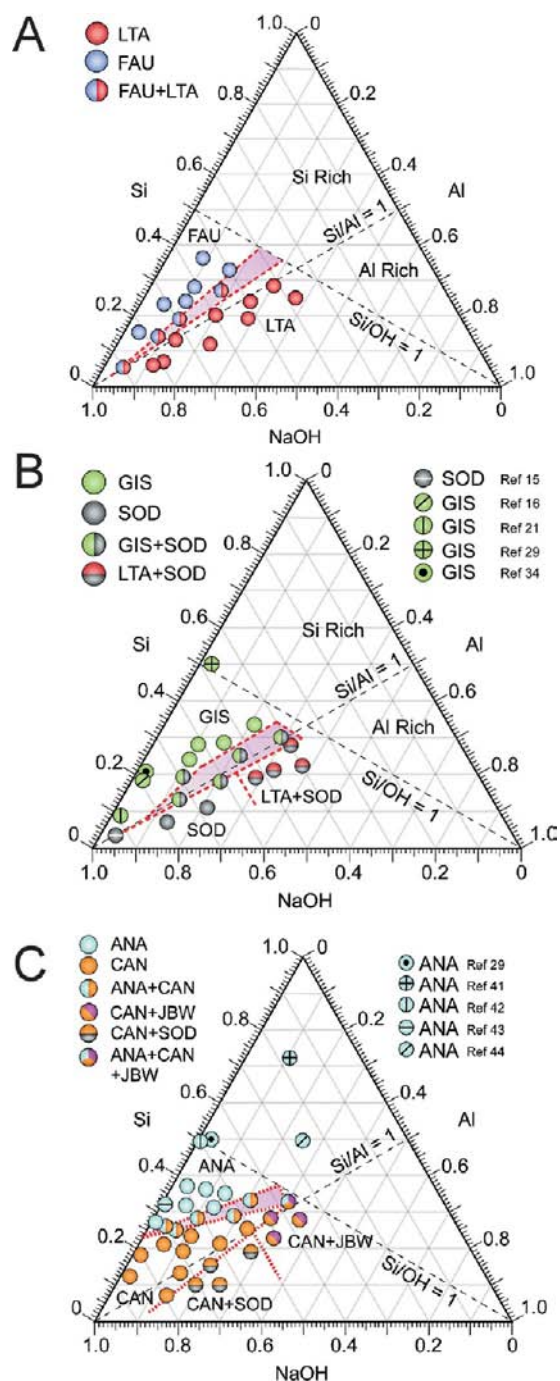
Figure 2. Kinetic ternary phase diagrams of zeolite structures showing single- and multi-phase (shaded) regions at increasing temperature: (A) LTA and FAU (65 °C, 7 days); (B) GIS and SOD (100 °C, 7 days) with a SOD−LTA binary region and a multiphase region with minor impurities; (C) CAN and ANA (180 °C, 21 days) with traces of JBW and SOD. The axes in the ternary diagrams are Si, Al, and NaOH mole fractions. The zeolite crystal structure(s) was confirmed using powder XRD. All synthesis solutions employed Na$^+$ as the extra-framework cation and a molar ratio 11 NaOH:190 H$_2$O (see Tables S3, S5, and S6 in the Supporting Information for details of the synthesis compositions).

prepare zeolite growth solutions. The hydroxide concentration is specified as NaOH to emphasize the use of Na$^+$ ions, which are introduced in equal concentration as hydroxide (the mineralizing agent). As previously mentioned, zeolites are

metastable relative to many natural silicates and aluminosilicates; therefore, if given enough time zeolites can transform to more stable structures. To this end, the ternary diagrams presented here are not thermodynamic phase diagrams but rather are kinetic phase diagrams that identify regions where single or multiphase pseudoequilibrium zeolite structures are formed at different synthesis time and temperature.

The ternary diagrams in Figure 2 compare the final zeolite crystal structures synthesized from growth solutions of molar composition X SiO$_2$:Y Al$_2$O$_3$:11 NaOH:190 H$_2$O at varying synthesis temperature. Here, we fixed the water content using a constant molar ratio of 11 NaOH:190 H$_2$O, which is an average value for Na-X (FAU-type) synthesis[31] (the influence of water content on zeolite crystallization will be discussed later). At low temperatures (e.g., 25−80 °C), FAU and LTA zeolites preferentially crystallize in Si- and Al-rich solutions, respectively. The phase diagram in Figure 2A highlights regions where pure FAU, pure LTA, and binary mixtures of FAU−LTA are formed after heating growth solutions at 65 °C for 7 days. The transition from pure LTA to pure FAU as SAR$_{(liq)}$ increases from 0.5 to 5 is evident in the XRD patterns of solids extracted from growth solutions (see Figure 1). These studies revealed a narrow multiphase region located around SAR$_{(liq)}$ = 1.2 (shaded area of Figure 2A).

As previously mentioned, our studies exclusively use Na$^+$ as the extra-framework cation; however, it should be noted that alkali and alkaline-earth metals can markedly influence zeolite crystallization.[32] For instance, Navrotsky et al.[23] showed that anhydrous M^{n+}-zeolites (with M^{n+} = Li$^+$, Na$^+$, K$^+$, Cs$^+$, Ca^{2+}, and Rb^{2+}) exhibit large disparity in the enthalpy of formation with changes in M^{n+}. Okubo and coworkers[15] examined the effect of substituting Na$^+$ with K$^+$ in FAU synthesis and observed the formation of low-silica zeolite X (LSX) in solutions of SAR$_{(liq)}$ = 1, which corresponds to a pure LTA region in Figure 2A. As such, it is reasonable to expect zeolite synthesis using cations other than Na$^+$ will alter the kinetic phase diagrams shown here. Analysis of different cations, however, is outside the scope of this current study.

Growth solutions were heated for 7 days to allow enough time for zeolite crystallization (although in many cases we observed that 1 to 3 days was more than sufficient). The extracted powders were analyzed by XRD and scanning electron microscopy (SEM). The latter can provide macroscopic validation of zeolite structures that exhibit distinct crystal habit. In certain cases, SEM may be used to determine if a minor impurity (not detectable by XRD) is present in the sample. For example, FAU and LTA zeolites have different crystal morphology. SEM images of FAU crystals reveal aggregates of spheroidal particles with sizes ranging from 10 to 50 nm (Figure 3A). Micrographs of LTA (Figure 3B) reveal much larger crystals (ca. 1 μm) with a distinct cubic habit. We observed small spheroidal particles in LTA samples with a size and shape closely resembling LTA crystals synthesized at 25 °C using similar compositions.[18] As such, it is possible that a fraction of LTA crystals did not grow large enough to develop distinct, observable facets. Conversely, these particles may be a minor fraction of FAU crystals that were not evident in the XRD pattern of this sample (see Figure 1,(a)). To this end, it is possible that growth solutions contain minor impurities (particularly compositions in close proximity to a phase boundary in the ternary diagram). Since we used XRD powder patterns in this study to index zeolite samples, the phase boundaries separating pure and multiphase regions are labeled
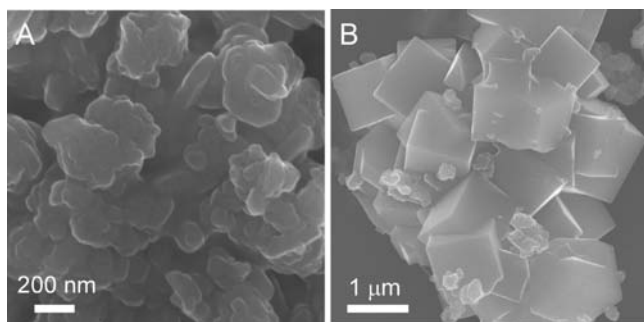
Figure 3. Scanning electron micrographs of zeolite crystals with framework types (A) FAU and (B) LTA prepared in Si-rich ($SAR_{(liq)}$ = 2.5) and Al-rich ($SAR_{(liq)}$ = 0.5) solutions, respectively, using 11 NaOH:190 H_2O solutions heated at 65 °C for 7 days. Aggregate sizes in (A) are consistent with a 150-nm hydrodynamic diameter measured by dynamic light scattering (DLS). We monitored the temporal changes in particle size using DLS, beginning with LUDOX (a colloidal suspension of 25-nm amorphous silica spheres). Upon addition of sodium aluminate to these solutions, aggregates formed and maintained a constant size over the course of FAU crystallization.

as dashed lines in ternary diagrams to emphasize that these divisions should be considered as approximate.

Šefčìk and McCormick[33] proposed a thermodynamic solution model (eq 1) to predict phase transitions between FAU and LTA using the solubility product, $\Pi_{s,i}$ (eq 2), for the condensation of silica and alumina to produce a zeolite of composition $NaAlSi_nO_{2n+2}$, where n is the silicon-to-aluminum ratio of the solid zeolite crystal or $SAR_{(s)}$. Šefčìk and McCormick reported that the solubility products of FAU and LTA decrease linearly with increasing $SAR_{(s)}$. They also reported that FAU and LTA exhibit similar $\Pi_{s,i}$ values in the range $1.0 < SAR_{(s)} < 1.3$, which can explain the observation of a binary region in the phase diagram.

$$n Si(OH)_4 + Al(OH)_4^- + Na^+$$
$$\overset{K_i}{\Leftrightarrow} NaAlSi_nO_{2n+2} + (n+2)H_2O \qquad (1)$$
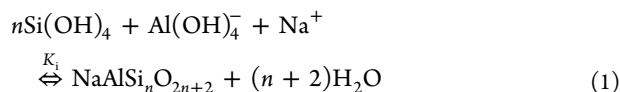
$$\prod_{s,i} = [Si(OH)_4]^n [Al(OH)_4^-][Na^+] \qquad (2)$$

A comparison of $\Pi_{s,i}$ for LTA and FAU zeolites suggests that the latter is more stable at higher $SAR_{(s)}$ due to its lower solubility product (i.e., $\Pi_{s,FAU} < \Pi_{s,LTA}$). Extrapolation of $\Pi_{s,i}$ data for FAU and LTA to $SAR_{(s)}$ values near the theoretical limit for zeolites, $SAR_{(s)} = 1$,[33] reveals a crossover point (i.e., $\Pi_{s,FAU} > \Pi_{s,LTA}$). This can explain why LTA is more thermodynamically stable than FAU in Al-rich solutions. Indeed, this hypothesis is consistent with the ternary phase diagram in Figure 2A comparing zeolite structures synthesized at different $SAR_{(liq)}$. The trends we observed for FAU and LTA synthesis at 65 °C agree with those predicted by Šefčìk and McCormick at 80 °C. The phase diagram in Figure 2A indicates that pure LTA is favored at $SAR_{(liq)} < 1.5$, and that a binary FAU-LTA region is observed in the approximate region $1.5 < SAR_{(liq)} < 2.5$. Phase boundaries reported here are qualitatively consistent with the theoretical boundaries predicted by Šefčìk and McCormick, with the exception that their multiphase region is narrower and centered around $SAR_{(liq)} = 1$.

Past studies have shown that a suspension of FAU crystals in growth solutions heated at elevated temperatures and/or for longer times can undergo a structural phase transformation to GIS-type zeolite.[16,21,34] Likewise, longer synthesis time can induce a structural transformation from LTA to SOD-type zeolite.[19,35] The fundamental mechanism of zeolite phase transformation is not fully understood. One hypothesis that has been proposed is that nucleation and growth of a new (more thermodynamically stable) crystal phase occurs heterogeneously on the exterior surface of the less thermodynamically stable crystal. A second hypothesis is that nucleation and growth of the second phase occurs homogeneously in solution.[36] In this current study, we do not infer which of these mechanisms is responsible for zeolite transformations, but rather our objective is to develop kinetic phase diagrams of zeolites wherein we analyze their pseudoequilibrium structures and not the intermediate stages during structural evolution.

To test the effect of temperature on the ternary phase diagram, we examined zeolites prepared at 100 and 180 °C. XRD analysis of zeolites prepared at 100 °C revealed the formation of GIS- and SOD-type frameworks in Si-rich and Al-rich solutions, respectively. The kinetic phase diagram (Figure 2B) highlights regions where pure GIS and SOD form after 7 days of hydrothermal treatment. Trends in the kinetic phase diagram are consistent with references (labeled on the diagram) that employed similar synthesis compositions and conditions (see Table S9 in SI). GIS-type zeolite (or zeolite P) is reported as an impurity in FAU syntheses that is formed at elevated temperature (ca. >200 °C) or longer synthesis time at lower temperatures.[16] Past studies of zeolite P have primarily focused on two objectives: (i) minimizing GIS formation in FAU syntheses[16] or (ii) achieving pure phases of maximum aluminum zeolite P (MAP)[37] with $SAR_{(s)} = 1$. To our knowledge, few studies have examined the synthesis of aluminosilicate zeolite P from organic-free systems.

GIS-type zeolite is a synthetic analogue of the naturally occurring gismondine, which has a flexible framework with two crystal polymorphs—cubic (referred to as P1) and tetragonal (P2).[37] A third phase (orthorhombic, P3), previously considered zeolite P, is now referred to as merlinoite (MER-type zeolite).[38] The crystal structure of zeolite P is similar to other framework types, such as ACO, APC, APD, ATT, and DFT, which share common building schemes (i.e. 8-membered ring (MR) pores in one plane interconnected by 1-dimensional crankshaft units).[39] It is difficult to distinguish P1 and P2 polymorphs from XRD powder patterns due to the similarity of their diffraction peaks. As such, we report crystals as being GIS-type and note that their XRD patterns (Figure S2 in SI) closely match those of zeolite P reported in the literature[40] and reference patterns of Na-GIS (Figure S7 in SI).[14]

The GIS-SOD multiphase region in Figure 2B (shaded area) lies within the range $0.8 < SAR_{(liq)} < 2$. This multiphase region is slightly larger than that of FAU–LTA in Figure 2A. The major phases within this region are GIS and SOD; however, several samples tested in the multiphase region contained a third phase in either trace or minor quantity (see Table S5 in SI), such as LTA (in Al-rich solutions), FAU (in Si-rich solutions), and CAN-type zeolite (in Si-rich solutions). In Al-rich solutions closer to molar ratios Si/OH = 1 we observed binary SOD–LTA mixtures, suggesting the LTA-to-SOD transformation is incomplete at the synthesis temperature and time chosen for these studies.

When the synthesis temperature was increased to 180 °C, we observed the formation of ANA- and CAN-type frameworks. For these studies, we increased the synthesis time to 21 days to allow adequate time for multiple structural transformations.

The kinetic phase diagram (Figure 2C) highlights regions where pure ANA and CAN form within 21 days of hydrothermal treatment. There is a notable change in the location of pure and multiphase regions in the ANA−CAN ternary diagram at 180 °C compared to phase diagrams at 65 °C (FAU−LTA, Figure 2A) and 100 °C (GIS−SOD, Figure 2B). The phase diagrams in A and B of Figure 2 contain triangular-shaped multiphase regions with phase boundaries defined by constant SAR$_{(liq)}$. For the ANA−CAN ternary diagram, we also observe a triangular-shaped multiphase region, but it is located along a diagonal that separates pure ANA and CAN phases in such a way that boundaries between pure and multiphase regions cannot be defined by a single Si/OH mole ratio or SAR$_{(liq)}$. Our studies revealed that pure ANA preferentially crystallizes at lower alkalinity. A comparison of our syntheses at molar ratios Si/OH < 1 with literature references of ANA synthesis[41−43] at Si/OH > 1 (labeled in Figure 2C) revealed excellent agreement within the phase diagram. Collectively, these studies indicate that pure ANA can be synthesized with higher Al content only at low alkalinity (e.g., Barrer et al.[44] report ANA with SAR = 2). As the alkalinity of the growth solution increases, we observed that the minimum SAR$_{(liq)}$ to achieve pure ANA crystals progressively increases, such that at Si/OH < 0.3 we no longer observed ANA crystallization. In Figure 2C, the maximum SAR$_{(liq)}$ value analyzed for ANA crystallization was 82.

CAN-type zeolite tends to crystallize in growth solutions with higher alkalinity than ANA. We observed the formation of CAN in both Si- and Al-rich solutions. At molar ratios Si/OH < 0.3, we observed CAN formation in Si-rich solutions (we tested SAR$_{(liq)}$ values as high as 8.3). In Al-rich solutions, we observed that SOD transformation to CAN is incomplete. The CAN−SOD binary phase region in Figure 2C was observed at SAR$_{(liq)}$ < 1. Interestingly, Al-rich solutions at lower alkalinity (i.e., close to a molar ratio Si/OH = 1) produced JBW-type zeolite (also known as Na-J). JBW has similar molar volume as ANA with a framework consisting of 1-D pores (Figure 4A) and jbw, abw, and dzc building units. SEM images of the JBW-CAN binary phase (Figure 4B) reveal the presence of large (20 to 150 μm) platelets with an elongated square bipyramidal morphology that closely resembles the crystal habit of highly crystalline Na-J reported by Lin et al.[45]

SEM images of the JBW−CAN binary phase revealed many small crystals with dimensions of 1 μm or less (e.g., inset of Figure 4B). These smaller particles exhibited diverse crystal habit, including spheroids of unknown structure, particles with bipyramid facets similar to larger JBW-type zeolite, and needlelike crystals that closely resemble SEM images of pure CAN crystals reported by Lin et al.[45] (additional SEM images of small crystals in the JBW−CAN sample are shown in Figure S13 in SI). In Figure 4C, we provide XRD patterns of solids extracted from the 180 °C synthesis (pattern ii) and simulated reference patterns of JBW and CAN (pattern i).[14] A comparison of experimental and simulated peaks confirms the presence of both zeolite crystal phases. The relative peak intensities suggest that CAN is the majority phase. Interestingly, other groups have reported the synthesis of pure JBW zeolite at the same location in the phase diagram, but using higher synthesis temperature (T ≥ 200 °C) and lower water content (11 NaOH:180 H$_2$O).[46] To this end, we performed our synthesis at 230 °C and compared its XRD pattern after 7 days of hydrothermal treatment (pattern iii) with the 180 °C synthesis. The higher-temperature synthesis still produces a
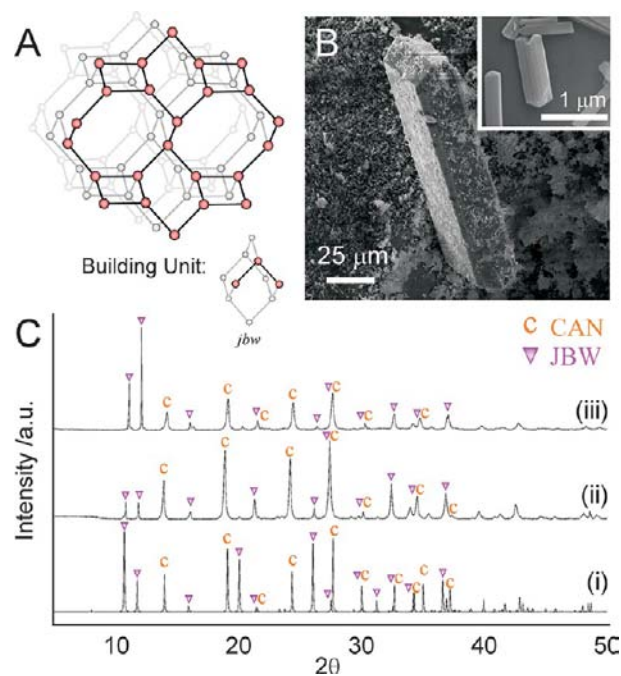

Figure 4. (A) JBW framework structure and its basic building unit, jbw. (B) Scanning electron micrograph of a JBW−CAN sample prepared with a solution of molar composition 6.9 SiO$_2$:3.5 Al$_2$O$_3$:11 NaOH:190 H$_2$O heated at 180 °C for 21 days. This synthesis yielded large faceted platelets (likely JBW-type crystals) and small needlelike crystals (inset) less than 1 μm in dimension. (C) XRD powder patterns of extracted solids from the 180 °C synthesis (ii) and a similar solution heated at 230 °C for 7 days (iii). Comparison of each experimental XRD pattern with the simulated patterns of JBW and CAN in (i) reveal a binary mixture of both phases. The relative shift in peak intensity between the two samples in (ii) and (iii) suggests that the fraction of JBW increases with increasing synthesis temperature.

binary JBW−CAN mixture, but a shift in the relative peak intensities of the XRD pattern suggests JBW is the majority phase at higher temperature. While it is apparent from this study that increased temperature promotes JBW formation, achieving a pure JBW phase would likely require the reduction of water content, 11 NaOH:Z H$_2$O (in the range 123 < Z < 190). The effect of water content on zeolite phase behavior will be discussed in a later section.

There are clear distinctions in the crystal habit of zeolites synthesized in different regions of the ternary phase diagrams. The size and morphology of zeolites that formed in Si-rich growth solutions (FAU, GIS, and ANA) were markedly different from each other. GIS and ANA crystals were much larger than FAU crystals. GIS zeolite (Figure 5A) forms 10-μm polycrystalline aggregates with remarkably uniform bipyramidal shape. Zeolite ANA (Figure 5B) formed 100-μm sized polyhedral crystals, which reportedly may contain polycrystalline interiors consisting of small ANA crystals tightly arranged into aggregates surrounded by a single-crystal exterior shell (for details of the core−shell structure, see the work of Chen et al.[47]). SEM images revealed that ANA polyhedra are fused together in what appears to be crystal intergrowths (see Figure S12C in SI) and/or aggregates that likely formed during the preparation of SEM samples.

Zeolites that crystallized in Al-rich solutions (LTA and SOD) tended to be smaller in size than those in Si-rich solutions (with the notable exception of JBW). As previously mentioned,
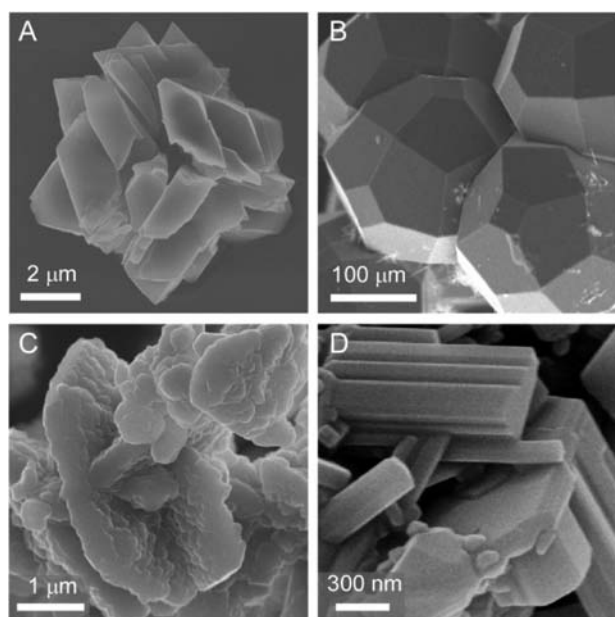
Figure 5. Scanning electron micrographs of zeolite crystals prepared in Si-rich solutions (A and B) and Al-rich solutions (C and D) with molar ratio 11 NaOH:190 H_2O. Solutions heated at 100 °C for 7 days produced GIS crystals (A: $SAR_{(liq)}$ = 2.5) and SOD crystals (C: $SAR_{(liq)}$ = 0.5). GIS zeolites are polycrystalline aggregates with bipyramidal morphology. SOD zeolites are dense particles that may be aggregates of smaller crystals, which is difficult to infer from SEM images. Solutions heated at 180 °C for 21 days produced ANA crystals (B: $SAR_{(liq)}$ = 13.7) and CAN crystals (D: $SAR_{(liq)}$ = 1.0). ANA zeolites have a polyhedral crystal habit with sizes exceeding 100 μm. CAN zeolites are a polydisperse mixture of platelet and rodlike crystal morphologies.

zeolite LTA forms faceted cubic crystals of 1-μm dimension. SOD forms dense particles (Figure 5C) lacking a distinct habit; however, the rough topography of these crystals is highly suggestive that SOD formation involves the aggregation of nanocrystals, which could not be uniquely identified in high resolution SEM images. CAN zeolite, which crystallizes in both Al-rich and Si-rich solutions, forms faceted crystals (Figure 5D) with polydisperse morphology that ranged from flat platelets to rodlike crystals of varying dimension (e.g., typically <1 μm in size).

Zeolite Phase Transformations. The transformation in zeolite structure with increasing temperature and/or synthesis time can be explained by Ostwald rule of stages—a phenomenon where kinetic pathways lead to the initial formation of a thermodynamically metastable structure that undergoes a series of recrystallization steps to form structures with progressively higher stability. These transformations occur by the gradual dissolution of one phase with simultaneous nucleation and growth of a second (more stable) phase. The progression of stages is determined by a combination of thermodynamic and kinetic factors. Here, we briefly review the thermodynamics of zeolite crystallization. Navrotsky and co-workers performed systematic calorimetric studies of zeolite formation for a wide variety of framework types and compositions (e.g., $SAR_{(s)}$, alkali cations, etc.).[23] They observed that the enthalpy of formation, ΔH_f, of anhydrous siliceous zeolites exhibits an approximate linear relationship with $\underline{V}$ (molar volume of zeolite framework structure) whereby the thermodynamic stability increases (i.e., ΔH_f becomes more

negative) with decreasing $\underline{V}$. This relationship was reported as $\underline{V}\alpha$ ($\Delta H_f - \Delta H^o$) (where ΔH^o = enthalpy of formation for quartz, which is used as a reference). These studies showed that a majority of zeolite frameworks exhibit similar ΔH_f, which may explain why kinetic factors play such an important role in determining the crystal structure. Indeed, a majority of zeolite framework types reported in the literature require an organic SDA to control the kinetics of aluminosilicate condensation to form specific rings, cages, and/or other characteristic subunits of the framework structure.

Table 1 lists the molar volumes for all zeolites discussed in this study. Assuming the proportionality $\underline{V}\alpha$ ($\Delta H_f - \Delta H^o$), we

Table 1. Crystal Structure Information of Zeolite Frameworks

zeolite	cell parameters (nm)			ring size (n-MR^a)	volume (cm^3/mol)
	a	b	c		
EMT	1.7215	1.7215	2.8082	12, 6, 4	45.3
FAU	2.4345	2.4345	2.4345	12, 6, 4	45.3
LTA	1.1919	1.1919	1.1919	8, 6, 4	42.4
GIS	0.9801	0.9801	1.0158	8, 4	36.7
SOD	0.8956	0.8956	0.8956	6, 4	36.1
CAN	1.2494	1.2494	0.5254	12, 6, 4	35.6
JBW	0.5256	0.7450	0.8159	8, 6, 4	32.0
ANA	1.3567	1.3567	1.3567	8, 6, 4	31.4

^{a}n-Membered ring where n is the number of tetrahedral atoms (Si or Al) along the circumference of the zeolite pore.

propose an Ostwald step rule in Figure 6 to describe phase transformations observed in ternary diagrams with increasing synthesis temperature and/or time. We observed general trends in zeolite structural transformations that followed the progressions of FAU-to-GIS-to-ANA in Si-rich solutions and LTA-to-SOD-to-CAN in Al-rich solutions. The zeolites formed at lower temperature (65 °C) were FAU or LTA, which have the highest molar volumes (i.e., low density frameworks), and are therefore the least thermodynamically stable structures. Both FAU and LTA are 3-D zeolites constructed from the same basic building unit, the sodalite cage (*sod*). In FAU, these cages are connected by double-six-membered rings (d6R), while the LTA framework consists of *sod* cages connected by double-four-membered rings (d4R) to produce *lta* cages (see Table S1 in SI for images of each basic building unit). The first structural transformation occurred at elevated temperature. For this study we selected 100 °C, which resulted in the FAU-to-GIS and LTA-to-SOD transformations. GIS and SOD have comparable molar volume, but very different crystal structures. SOD is a 0-D zeolite formed by the connection of *sod* building units, whereas GIS is a 3-D zeolite constructed from *gis* and *dcc* building units.

The second transition occurred at even higher temperature. For this study we selected 180 °C as the synthesis temperature and increased the synthesis time by a factor of 3 to allow sufficient time for structural transformations. The zeolites formed at these conditions were primarily ANA and CAN, which exhibit markedly different crystal topology. CAN is comprised of 1-D channels derived from the connection of *can* and *dzc* building units. ANA forms an interconnected 3-D network of channels (without any identified building unit) that is difficult to convey in a 2-D drawing. As such, we highlighted
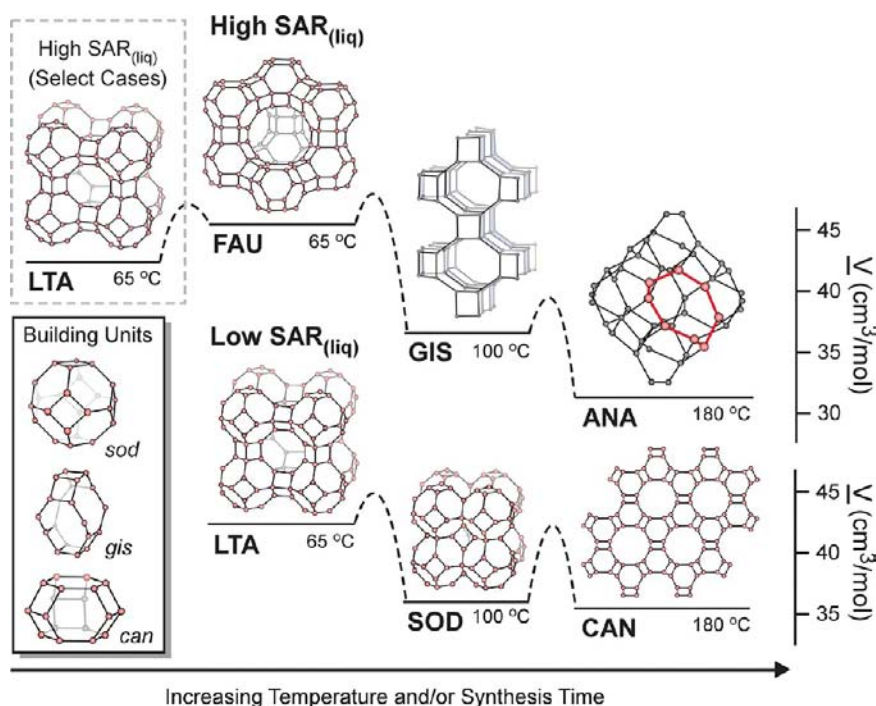
Figure 6. Stages of Na-zeolite phase transformation with increasing synthesis temperature and/or time. These transitions are consistent with Ostwald's rule of stages wherein metastable structures progressively transform to more thermodynamically stable structures. The relative enthalpy of formation, $\Delta H_f - \Delta H^{\circ}$, for anhydrous zeolite structures is assumed to be proportional to its molar volume, $\underline{V}$. The sequence of stages progresses from low to high density structures (i.e., increasing thermodynamic stability). The stages shown here are based on trends observed in Figure 2 (solutions with molar ratio 11 NaOH:190 H_2O). Phase transformations in Si-rich solutions (ca. $SAR_{(liq)} > 2$) tend to follow the sequence FAU→GIS →ANA. In select cases, we observed an initial LTA→FAU transformation (dashed box). Phase transformations in Al-rich solutions (ca. $SAR_{(liq)} < 1$) tend to follow the sequence LTA→SOD→CAN. (Inset) Characteristic building units of these zeolite structures (*sod*, *gis*, and *can*). See Table S1 (SI) for a full list of all building units.

one pore opening in Figure 6 (red line) to aid the visualization of its crystal structure.

It is important to mention that the schematic in Figure 6 is specific for synthesis compositions in Figure 2 using a molar ratio of 11 NaOH:190 H_2O. Although the structural transformations FAU-to-GIS-to-ANA and LTA-to-SOD-to-CAN depicted in Figure 6 are common, they were not observed at all $SAR_{(liq)}$ values in the phase diagrams. Notable exceptions to the sequence of stages depicted in Figure 6 include (i) the formation of CAN in Si-rich solutions at high alkalinity (i.e., low Si/OH mole ratio) in Figure 2C; (ii) the formation of an additional structure, EMT-type zeolite, in growth solutions with low water content (e.g., molar ratio of 11 NaOH:66 H_2O); (iii) the formation of SOD in Si- and Al-rich regions of the phase diagram for growth solutions with low water content; and (iv) a LTA-to-FAU transformation at $SAR_{(liq)} > 2$ in Figure 2A. Here, we will discuss the first point and address the remaining points in the following two sections.

Inspection of Figure 2C reveals that the transformation from GIS to ANA occurs at Si/OH > 0.3. In more alkaline solutions (i.e., bottom left corner of the ternary diagram) we observed a transformation from GIS to CAN. It is not evident if these transformations are primarily driven by thermodynamic or kinetic factors. On the basis of molar volume, ANA is expected to be more thermodynamically stable than CAN (i.e., $\underline{V}_{ANA} < \underline{V}_{CAN}$), which suggests kinetic factors play a dominant role in the phase selection of CAN; however, the relationship between molar volume and enthalpy of formation used in Figure 6 to explain the Ostwald step rule is an oversimplification that we adapted from the aforementioned calorimetry study of all-silica

zeolites. As such, our approximation neglects the effect of framework aluminum, $SAR_{(s)}$, which has been shown to have a significant impact on zeolite ΔH_f.[23] One technique that in theory could be used to examine the thermodynamics of phase transformation is *in situ* calorimetry, which has proven useful for probing thermal events in zeolite synthesis. However, *in situ* calorimetric studies of SOD formation performed by Liu and Navrotsky[48] revealed no calorimetric signal associated with the phase transformation from LTA to SOD. They suggested that the difference in ΔH_f between LTA and SOD is too small (i.e., < 1 kJ/mol) to distinguish by *in situ* calorimetry, despite the relatively large difference in $\underline{V}$ of these two zeolite structures.

Observations made in this study and by others suggest that predicting pseudoequilibrium phases in ternary diagrams *a priori* is challenging. Itabashi et al.[28] proposed a hypothesis that zeolite crystallization in seeded organic-free syntheses occurs when the gel solution and the framework type share a common building unit. Nonseeded phase transformations among LTA, FAU, and SOD framework types are consistent with this theory; however, the FAU-to-GIS, GIS-to-ANA, and SOD-to-CAN transformations involve structures of disparate building units, suggesting a common structural subunit is not a prerequisite for zeolite phase transformations. There are methods for modeling zeolite phase behavior, such as the solution model (eq 1) that uses the solubility products of aluminosilicate zeolites to approximate pure and multiphase regions of ternary phase diagrams. Šefčik and McCormick used this model to calculate a theoretical FAU−LTA phase diagram similar to the one in Figure 2A. It is reasonable to suggest this model could also be applied to the GIS−SOD diagram in

Figure 2B, which exhibits similar phase behavior. However, model calculations of Figure 2C containing multiple framework types (i.e., ANA, CAN, JBW, etc.) may prove to be more challenging, given its greater complexity relative to the other ternary phase diagrams.

Constructing Phase Diagrams in Six-Dimensions. The kinetic phase diagrams in A–C of Figure 2 illustrate the effects of four parameters. A single ternary diagram accounts for three dimensions, which are the mole fractions of silicon, aluminum, and hydroxide. The fourth dimension was the temperature of hydrothermal treatment. Two additional parameters not explicitly investigated in Figure 2 were synthesis time (i.e., the duration of hydrothermal treatment) and the water content, which we refer to as the NaOH:H_2O molar ratio. Here, we performed tests at varying synthesis time and water content to extend the kinetic phase diagrams by two additional dimensions.

We will first discuss the influence of synthesis time. The phase diagrams in Figure 2 are based on zeolite structures that formed after some predetermined duration of hydrothermal treatment. For these studies, we selected 7 days for the synthesis of zeolites with lower framework density, which included FAU, LTA, GIS, and SOD. For zeolites with higher density (i.e., ANA, CAN, and JBW), we increased the synthesis time to 21 days. As previously mentioned, these times were much longer than needed in many instances, but they were selected to provide sufficient time for observing structural transformations. Since the transformation from one zeolite structure to another occurs by concerted processes involving the dissolution of the less stable phase and nucleation and growth of the more stable phase, the exact time required for complete transformation depends on the relative rates of dissolution and crystallization of each structure.

Time and temperature have very similar effect on zeolite phase transformations. As such, we present the progression of stages in Figure 6 as an increase in either parameter. For instance, the synthesis of pure zeolites can be accomplished using either a long synthesis time at low temperature or a higher temperature with shorter synthesis time. This provides some flexibility in the design of pure zeolites for achieving an optimal balance between convenience (i.e., less time) and economics (i.e., low temperature). We observed that subtle adjustments in temperature can lead to significant changes in crystal products, which we demonstrate here using a composition in Figure 2B that produced a binary GIS–SOD mixture with trace amounts of FAU. When we reduced the synthesis temperature from 100 to 95 °C, XRD patterns of solids extracted at periodic times (Figure 7) during the synthesis revealed as few as one and as many as four crystal phases present at any given time. After 7 days of hydrothermal treatment, we observed a three-phase GIS–SOD–FAU mixture where FAU was present in greater quantity. This study suggests that not enough time was allowed for the complete transformation from FAU to GIS. In a separate experiment, we increased the temperature of the growth solution to 120 °C, and after 7 days of hydrothermal treatment we obtained a three phase GIS–SOD–CAN mixture (see Figure S8 in SI). The same composition heated at 180 °C for 21 days resulted in pure CAN (Figure 2C). Collectively, these studies reveal that the judicious selection of synthesis temperature and time is important for tailoring zeolite phase purity.

The sixth parameter we tested was water content. Changing the amount of water in zeolite growth solutions alters the
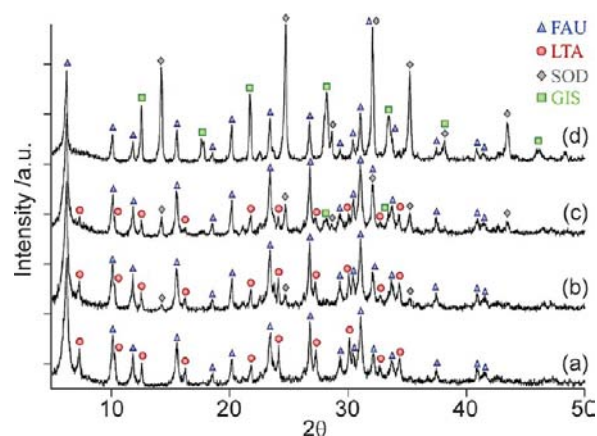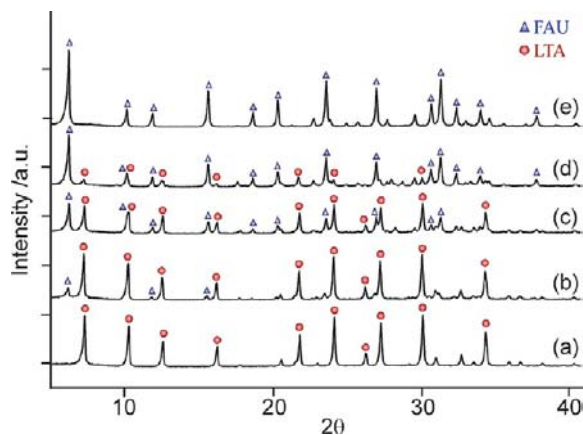

Figure 7. Powder XRD patterns of solids extracted from growth solutions with molar composition 3 SiO_2:0.5 Al_2O_3:11 NaOH:190 H_2O ($SAR_{(liq)}$ = 1.5) heated at 95 °C for (a) 24 h, (b) 48 h, (c) 72 h, and (d) 168 h. This composition yields a FAU–LTA binary mixture at lower temperature (65 °C, Figure 2A) and a GIS–SOD binary mixture at higher temperature (100 °C, Figure 2B). At the intermediate temperature shown here, the transformations LTA-to-SOD and FAU-to-GIS are incomplete. As such, XRD spectra reveal as few as one and as many as four different crystal phases during the course of hydrothermal treatment.

concentrations of SiO_2 and Al_2O_3 and may (but not necessarily) alter the solution pH (see Tables S2–S8 in SI for pH values of all experiments in this study). We tested the effect of water content by adjusting the NaOH:H_2O molar ratio of the growth solution. Recall that the kinetic phase diagrams in A–C of Figure 2 were constructed at fixed molar ratio 11 NaOH:190 H_2O and varying temperature. Here, we kept time and temperature fixed at 7 days and 65 °C, and we examined the effect of higher water content (11 NaOH:348 H_2O) and lower water content (11 NaOH:66 H_2O). The ternary phase diagrams in Figure 8 are plotted vertically (bottom to top) from high to low water content. The middle ternary diagram is Figure 2A redrawn without the individual data points. The bottom ternary diagram at higher water content shows the effect of reducing the concentrations of SiO_2 and Al_2O_3 by nearly one-half. Syntheses at higher water content produced a FAU–LTA phase diagram similar to the one in Figure 2A, but with a larger multiphase region (see Figure S10 in SI for a more detailed phase diagram). Comparison of XRD patterns in Figure 9 (at higher water content) with those in Figure 1 (at lower water content) reveal that the two-phase region of the former spans a broader range of $SAR_{(liq)}$ values (i.e., from 1 to 2).

Interestingly, we observed that decreasing the water content (Figure 8, top diagram) dramatically shifts the phase behavior to pure SOD. Similar transformations were observed at an intermediate water content, i.e. 11 NaOH:95 H_2O (see Figure S6 in SI). These results are qualitatively consistent with those reported by Subotić and co-workers[50] and Valtchev et al.,[18] who observed a LTA-to-SOD transformation with reduced water content at $SAR_{(liq)} \approx 1$. Our results indicate that the shift in phase behavior from a FAU–LTA diagram to one of pure SOD occurs at a molar ratio 11 NaOH:Z H_2O where Z is between 95 and 123. Moreover, we observed that syntheses with low water content form gels at low alkalinity (i.e., molar ratios Si/OH > 0.4). This region is highlighted in Figure 8 (a more detailed ternary diagram is provided in Figure S11 in SI).
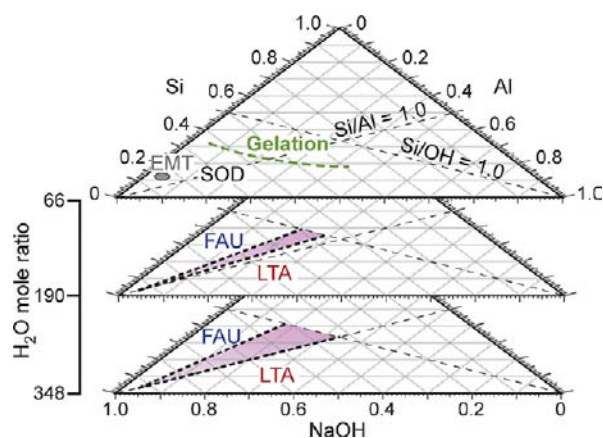
Figure 8. Kinetic phase diagrams for zeolite growth solutions at varying water content heated for 7 days at 65 °C. (*Bottom*) High water content solutions (11 NaOH:348 H_2O) yield a FAU−LTA phase diagram with a large binary region (shaded area). (*Middle*) Solutions with moderate water content (11 NaOH:190 H_2O) yield a FAU−LTA phase diagram (identical to Figure 2A) with a narrow binary region. (*Top*) Low water content solutions (11 NaOH:66 H_2O) yield a SOD phase diagram that spans both Si- and Al-rich regions and a gelation region at low alkalinity (dashed line indicates the approximate gelation boundary). The composition used by Ng et al.[49] to produce pure EMT at 30 °C (36 h heating) is labeled (circle). Detailed phase diagrams of the bottom and top ternary plots are provided in Figures S10 and S11 in SI.

Figure 9. XRD patterns of solids extracted from growth solutions with molar composition 11 NaOH:348 H_2O heated at 65 °C for 7 days. The crystalline products (LTA and/or FAU) were obtained using the following $SAR_{(liq)}$ values: (a) LTA, 0.9; (b) LTA−FAU, 1.0; (c) LTA−FAU, 1.5; (d) FAU−LTA, 2.0; and (e) FAU, 4.0.

The gels form immediately upon mixing silica and alumina at 25 °C, but with continued stirring they become viscous slurries. We did not perform systematic studies of the gelation region; however, we did examine several gels heated at 65 °C for 7 days and observed multiphase regions—notably a three-phase SOD−GIS−FAU region in close proximity to the gel boundary and a two-phase GIS−FAU region at lower alkalinity (closer to a molar ratio Si/OH = 1).

Ng et al. reported the synthesis of EMT-type zeolite at conditions similar to ours, but using growth solutions with a molar ratio 11 NaOH:70 H_2O (with $SAR_{(liq)}$ = 2.5), reduced heating time, and lower temperature (i.e., 36 h at 30 °C).[49] As shown in Figure 10A, the EMT framework contains a 3-D network of pores formed by interconnected *sod* and *d6R*
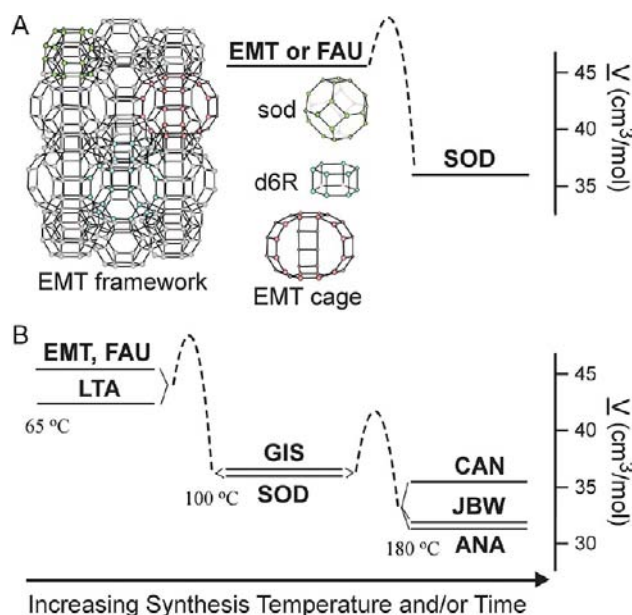
Figure 10. (A) Zeolite structural transformations at low water content (11 NaOH:Z H_2O, with Z < 105). Growth solutions heated at 65 °C for short times produce FAU or EMT.[49] The molar volume of both structures is equal. At increased synthesis temperature and time, FAU and/or EMT transform to SOD. (B) Zeolite structural transformations at high water content (11 NaOH:Z H_2O, with Z ≥ 190). The sequence of stages can differ from those depicted in Figure 6. At the earliest stage, the first structures to nucleate are LTA, FAU, or EMT; and at the final stage, the structures are ANA, CAN, or JBW (depending on the composition). If we also account for potential intermediate structures, such as GIS and SOD, there are 12 or more possible sequences for phase transformations at the synthesis conditions studied here.

building units. Synthesizing EMT without an organic SDA has proven to be challenging. Mintova and co-workers elegantly showed that EMT crystallizes in organic-free media at low temperature and short synthesis time. Preliminary studies in our group suggest that EMT can be prepared using a combination of higher temperature and shorter synthesis time. We reproduced the EMT synthesis at 65 °C, and after 2 h of heating the XRD pattern of solids extracted from the growth solution (Figure S5 in SI) was similar to the EMT pattern reported by Ng et al.[49] Within 4 h of heating, XRD patterns contained pure SOD without any trace of EMT (Figure S4 in SI), which is qualitatively consistent with the EMT-to-SOD transformation reported by Ng et al. for longer heating times at 30 °C. Our results show that, among the conditions considered, i.e. low temperature and water content, the latter is most critical for EMT formation.

Initial Stage of Zeolite Crystallization. We previously mentioned that the Ostwald stages of zeolite transformation depicted in Figure 6 are based on general observations made from syntheses using moderate water content. Results presented in the previous section reveal that the progression of stages is influenced by the water content (most notably at the initial stage of zeolite nucleation). Figure 10A depicts the Ostwald rule of stages observed for syntheses at low water content. Growth solutions with molar composition 11 NaOH:66 H_2O initially form EMT or FAU, which then transform to SOD at longer synthesis time. SOD formation was observed in both Si- and Al-rich regions of the phase diagram, which is contrary to its formation in only Al-rich solutions at

higher water content (Figure 2B). Moreover, SOD formation at low water content occurs at much lower temperature and synthesis time. For instance, SOD forms at 65 °C after several hours in growth solutions with low water content compared to several days at 100 °C with high water content.

Mintova and co-workers reported that solutions with a molar ratio of 11 NaOH:110 H_2O initially form EMT, but transform to FAU with increased synthesis time. EMT and FAU structures have identical molar volume (see Table 1), which suggests their enthalpies of formation are similar. Indeed, the structures EMT, FAU, and SOD are derived from the same *sod* building unit,[49] which may explain why subtle differences in zeolite synthesis conditions have a significant impact on the possible pathways for structural transformation, which include EMT-to-SOD, FAU-to-SOD, or EMT-to-FAU-to-SOD. The molar ratio 11 NaOH:Z H_2O that defines whether the growth solution is low or high water content is not apparent from these studies. This distinction may be loosely defined around a narrow region of SAR$_{(liq)}$. On the basis of observations made here and those reported by other groups, the transition from high-to-low water content seemingly occurs at $110 < Z < 190$. For instance, the initial zeolite structures observed in syntheses at $Z \leq 110$ differ from those at $Z \geq 190$.

In Figure 6, we showed that one of the initial structures that can form in Si-rich growth solutions is LTA (a framework structure that typically forms in Al-rich solutions). The LTA-to-FAU transformation seemingly contradicts the trend predicted by the Ostwald rule of stages since this sequence involves a switch from a larger density structure to one that is less dense, and hence less thermodynamically stable. Herein, we provide an explanation for this anomaly and discuss why an LTA-to-FAU transformation can occur in Si-rich regions of Figure 2A. Growth solutions used in this study employed the silica source LUDOX, which is a colloidal suspension of amorphous spherical silica particles (∼25-nm diameter). Breck was one of the first to propose that mixtures of silicon and aluminum sources in basic solutions yield gels with composition $Na_a(AlO_2)_b(SiO_2)_c \cdot NaOH \cdot H_2O$ that form via a condensation–polymerization mechanism between silicate and aluminate species.[12] We observed, however, that growth solutions aged at room temperature for 48 h still contained amorphous silica particles (Figure 11A). The silica particles did not completely dissolve, even after several hours of heating at 65 °C (Figure S14 in SI). Transmission electron micrographs revealed the presence of ∼30 nm spherical particles (Figure 11B). We performed a systematic investigation of these particles, which revealed a core–shell structure comprising a Si core (with similar diameter as LUDOX particles) and an Al-rich shell. Details of the core–shell structure are outside the scope of this study but will be reported as a followup to this work.

Collectively, these results suggest that zeolite nucleation in Si-rich regions of the phase diagram occur in an environment that is not representative of the overall molar composition of the growth solution. Instead, the solution resembles compositions used in the Al-rich region of the phase diagram since a majority of silica within the LUDOX particles is inaccessible to the solution. As such, these synthesis solutions can lead to the initial formation of LTA, followed by its transformation to FAU as the growth solution becomes enriched with silica. XRD patterns of solids extracted at periodic times during a 65 °C synthesis (Figure 11C) clearly show an amorphous-to-LTA-to-FAU progression of stages. The final stage of this sequence after 7 days of heating is consistent with our observation in
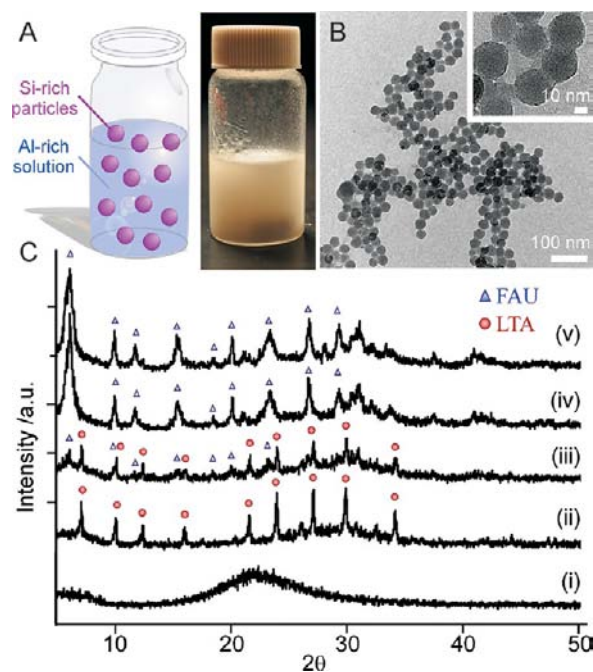
Figure 11. Inhomogeneous growth solutions arising from the use of colloidal silica sources can lead to the initial formation of LTA in Si-rich regions of the phase diagram. Here we refer to growth solutions with a molar composition 4.0 SiO$_2$:1.0 Al$_2$O$_3$:11 NaOH:190 H$_2$O aged at room temperature. (A) LTA nucleation can occur in Al-rich solutions when the majority of silica is retained within the 25-nm LUDOX particles. The picture of the sol−gel solution was taken after 24 h of aging at room temperature. (B) TEM image at low and high (inset) magnification of particles extracted after 48 h of aging. Micrographs reveal that solutions contain spheroidal particles with sizes similar to those of LUDOX reagent. (C) Powder XRD patterns of solids extracted at periodic times from the same growth solution heated at 65 °C for (i) 0 h, (ii) 6 h, (iii) 12 h, (iv) 24 h, and (v) 7 days. These studies showed the onset of LTA crystals after 6 h of heating, and a complete LTA-to-FAU transformation within 24 h.

Figure 2A that FAU preferentially crystallizes in Si-rich regions of the phase diagram.

Preliminary studies in our group seem to indicate that LTA formation in Si-rich growth solutions is more the exception than the norm, since FAU was more commonly observed as the initial phase. The LTA-to-FAU transformation in Figure 11 pertains to a growth solution with SAR$_{(liq)}$ = 2.5, which is close to the multiphase boundary in Figure 2A. Other groups, such as Valtchev and co-workers, have reported FAU nucleation at the same SAR$_{(liq)}$, but at a composition with higher alkalinity (identical to the EMT synthesis in Figure 8) and higher water content (i.e., 11 NaOH:261 H$_2$O). To this end, more rigorous studies at short synthesis times are required to identify the initial structures formed in different regions of the phase diagram. It is evident from our studies, though, that structural transformations exhibit multiple pathways based on the composition and/or water content of the growth solution. The sequence of stages at low water content (Figure 10A) is quite different than those at high water content (Figure 6). Moreover, there are many alternative pathways, such as those illustrated in Figure 10B for zeolite structures observed in this study. The transformations in zeolite structure differ from region to region within phase diagrams, and the possible combinations of sequences could potentially include additional framework types not observed here (i.e., structures that may

form at intermediate synthesis times or temperatures not analyzed in this study). Indeed, we anticipate that future studies will uncover new phase transformations and expand upon the kinetic phase diagrams presented here to broaden the parameter space for synthesizing zeolites with pure crystal phases.

CONCLUSIONS

While the phenomenon of crystal phase transformation in zeolite synthesis in the absence of organics or crystal seeds has been well-documented, a generalized framework for quantifying phase behavior at different synthesis conditions has been lacking. Here, we present a platform that permits the facile, unambiguous identification of zeolite synthesis compositions and conditions for the formation of phase-pure structures. This study draws inspiration from the pioneering work of Breck, Flanigen, and others who formulated empirical trends using $SiO_2-Al_2O_3-Na_2O$ ternary diagrams. To our knowledge, this is the first quantitative analysis of such diagrams for zeolite synthesis, which may prove useful for identifying a parameter space for tailoring crystal composition (i.e., changes in $SAR_{(s)}$) and properties (e.g., crystal size and habit) without sacrificing phase purity. This approach is a significant step toward rational zeolite design, which collectively seeks to improve upon the costly and time-consuming empirical approaches of zeolite synthesis, while optimizing their performance for commercial applications. In this study, we constructed phase diagrams for organic-free syntheses of Na-zeolites through careful consideration of six parameters: three compositions (Si–Al–NaOH mole fractions), water content, temperature, and time. We propose that trends in zeolite phase transformation are consistent with the Ostwald rule of stages, which is a common mechanism attributed to crystal polymorphism in areas such as pharmaceuticals, biomineralization, and ceramics. There are few examples of crystals capable of undergoing more than two polymorphic transitions. Interestingly, we show in this study that Na-zeolites can undergo three or more distinct phase transformations.

This study only addresses a fraction of the available parameter space for zeolite synthesis. A comprehensive analysis of zeolite phase behavior is nontrivial given the number of possible parameter combinations that must be considered. Additional parameters include the selection of reagents (e.g., Si and Al sources) and extra-framework cations. It is also likely that syntheses using water content, $SAR_{(liq)}$, alkalinity (Si/OH mole ratio), and temperature outside the ranges examined here will reveal additional crystal structures and/or phase behavior. Here, we discussed the formation of eight zeolite framework types in organic-free synthesis, but many other structures can form under similar conditions. Examples include (but are not limited to) zeolite framework types MFI, CHA, LTL, and MOR. This list can be further expanded if organic SDAs are included as an additional design parameter. To this end, we envision that the approach presented here has broader applicability and can be extended to the aforementioned crystal structures and synthesis conditions in the future.

ASSOCIATED CONTENT

Ⓢ Supporting Information

Synthesis compositions for kinetic phase diagrams and their XRD powder patterns; detailed phase diagrams of Figure 8 (top and bottom ternary plots); additional electron microscopy (SEM and TEM) images. This material is available free of charge via the Internet at http://pubs.acs.org.

AUTHOR INFORMATION

Corresponding Author
jrimer@central.uh.edu

Author Contributions
‡M.M and M.D.O. have contributed equally to this paper.

Notes
The authors declare no competing financial interest.

REFERENCES

(1) Martinez, C.; Corma, A. *Coord. Chem. Rev.* **2011**, *255*, 1558.
(2) Colombo, M.; Nova, I.; Tronconi, E. *Catal. Today* **2010**, *151*, 223.
(3) Roy, S.; Baiker, A. *Chem. Rev.* **2009**, *109*, 4054.
(4) Jae, J.; Tompsett, G. A.; Foster, A. J.; Hammond, K. D.; Auerbach, S. M.; Lobo, R. F.; Huber, G. W. *J. Catal.* **2011**, *279*, 257.
(5) Bomgardner, M. M. *Chem. Eng. News* **2011**, *89*, 20.
(6) Choi, M.; Na, K.; Kim, J.; Sakamoto, Y.; Terasaki, O.; Ryoo, R. *Nature* **2009**, *461*, 246.
(7) Na, K.; Jo, C.; Kim, J.; Cho, K.; Jung, J.; Seo, Y.; Messinger, R. J.; Chmelka, B. F.; Ryoo, R. *Science* **2011**, *333*, 328.
(8) Lai, Z.; Bonilla, G.; Diaz, I.; Nery, J. G.; Sujaoti, K.; Amat, M. A.; Kokkoli, E.; Terasaki, O.; Thompson, R. W.; Tsapatsis, M.; Vlachos, D. G. *Science* **2003**, *300*, 456.
(9) Zhang, X. Y.; Liu, D. X.; Xu, D. D.; Asahina, S.; Cychosz, K. A.; Agrawal, K. V.; Al Wahedi, Y.; Bhan, A.; Al Hashimi, S.; Terasaki, O.; Thommes, M.; Tsapatsis, M. *Science* **2012**, *336*, 1684.
(10) Larlus, O.; Valtchev, V. P. *Chem. Mater.* **2004**, *16*, 3381.
(11) Zhang, L.; van Laak, A. N. C.; de Jongh, P. E.; de Jong, K. P. *Microporous Mesoporous Mater.* **2009**, *126*, 115.
(12) Breck, D. W. *Zeolite Molecular Sieves: Structure, Chemistry, and Use*; Wiley: New York, 1973.
(13) Barrer, R. M.; White, E. A. D. *J. Chem. Soc.* **1952**, 1561.
(14) International Zeolite Association, www.iza-online.org.
(15) Iwama, M.; Suzuki, Y.; Plevert, J.; Itabashi, K.; Ogura, M.; Okubo, T. *Cryst. Growth Des.* **2010**, *10*, 3471.
(16) Osada, M.; Sasaki, I.; Nishioka, M.; Sadakata, M.; Okubo, T. *Microporous Mesoporous Mater.* **1998**, *23*, 287.
(17) Khajavi, S.; Sartipi, S.; Gascon, J.; Jansen, J. C.; Kapteijn, F. *Microporous Mesoporous Mater.* **2010**, *132*, 510.
(18) Valtchev, V. P.; Tosheva, L.; Bozhilov, K. N. *Langmuir* **2005**, *21*, 10724.
(19) Huang, Y.; Yao, J.; Zhang, X.; Kong, C.; Chen, H.; Liu, D.; Tsapatsis, M.; Hill, M. R.; Hill, A. J.; Wang, H. *CrystEngComm* **2011**, *13*, 4714.
(20) Krznaric, I.; Antonic, T.; Bronic, J.; Subotic, B.; Thompson, R. W. *Croat. Chem. Acta* **2003**, *76*, 7.
(21) Ogura, M.; Kawazu, Y.; Takahashi, H.; Okubo, T. *Chem. Mater.* **2003**, *15*, 2661.
(22) Basaldella, E. I.; Tara, J. C. *Zeolites* **1995**, *15*, 243.
(23) Navrotsky, A.; Trofymluk, O.; Levchenko, A. A. *Chem. Rev.* **2009**, *109*, 3885.
(24) Navrotsky, A. *Proc. Natl. Acad. Sci. U.S.A.* **2004**, *101*, 12096.
(25) Lobo, R. F.; Zones, S. I.; Davis, M. E. *J. Incl. Phenom. Mol. Recognit. Chem.* **1995**, *21*, 47.

(26) Kecht, J.; Mintova, S.; Bein, T. *Microporous Mesoporous Mat.* **2008**, *116*, 258.

(27) Subotic, B.; Smit, I.; Madzija, O.; Sekovanic, L. *Zeolites* **1982**, *2*, 135.

(28) Itabashi, K.; Kamimura, Y.; Iyoki, K.; Shimojima, A.; Okubo, T. *J. Am. Chem. Soc.* **2012**, *134*, 11542.

(29) Zones, S. I.; Vannordstrand, R. A. *Zeolites* **1988**, *8*, 166.

(30) Zones, S. I. *J. Chem. Soc., Faraday Trans.* **1991**, *87*, 3709.

(31) Zhan, B. Z.; White, M. A.; Lumsden, M.; Mueller-Neuhaus, J.; Robertson, K. N.; Cameron, T. S.; Gharghouri, M. *Chem. Mater.* **2002**, *14*, 3636.

(32) Auerbach, S. M.; Carrado, K. A.; Dutta, P. K. *Handbook of Zeolite Science and Technology*; M. Dekker: New York, 2003.

(33) Šefčík, J.; McCormick, A. V. *Chem. Eng. Sci.* **1999**, *54*, 3513.

(34) Dwyer, F. G.; Chu, P. *J. Catal.* **1979**, *59*, 263.

(35) Greer, H.; Wheatley, P. S.; Ashbrook, S. E.; Morris, R. E.; Zhou, W. *J. Am. Chem. Soc.* **2009**, *131*, 17986.

(36) Cundy, C. S.; Cox, P. A. *Microporous Mesoporous Mater.* **2005**, *82*, 1.

(37) Albert, B. R.; Cheetham, A. K.; Stuart, J. A.; Adams, C. J. *Microporous Mesoporous Mater.* **1998**, *21*, 133.

(38) Nery, J. G.; Mascarenhas, Y. P.; Cheetham, A. K. *Microporous Mesoporous Mater.* **2003**, *57*, 229.

(39) Baur, W. H.; Fischer, R. X. *J. Chem. Soc., Dalton Trans.* **2002**, 630.

(40) Huang, Y.; Dong, D. H.; Yao, J. F.; He, L.; Ho, J.; Kong, C. H.; Hill, A. J.; Wang, H. T. *Chem. Mater.* **2010**, *22*, 5271.

(41) Agger, J. R.; Shoaee, M.; Mistry, M.; Slater, B. *J. Cryst. Growth* **2006**, *294*, 78.

(42) Tatlier, M.; Baris, K.; Tokay, C. B.; Erdem-Senatalar, A. *J. Cryst. Growth* **2007**, *306*, 146.

(43) Wiersema, G. S.; Thompson, R. W. *J. Mater. Chem.* **1996**, *6*, 1693.

(44) Barrer, R. M.; Marcilly, C. *J. Chem. Soc. A* **1970**, 2735.

(45) Lin, D. C.; Xu, X. W.; Zuo, F.; Long, Y. C. *Microporous Mesoporous Mater.* **2004**, *70*, 63.

(46) Healey, A. M.; Johnson, G. M.; Weller, M. T. *Microporous Mesoporous Mater.* **2000**, *37*, 153.

(47) Chen, X.; Qiao, M.; Xie, S.; Fan, K.; Zhou, W.; He, H. *J. Am. Chem. Soc.* **2007**, *129*, 13305.

(48) Liu, Q.; Navrotsky, A. *Geochim. Cosmochim. Acta* **2007**, *71*, 2072.

(49) Ng, E. P.; Chateigner, D.; Bein, T.; Valtchev, V.; Mintova, S. *Science* **2012**, *335*, 70.

(50) Bosnar, S.; Bronic, J.; Jelic, T. A.; Subotic, B. *CrystEngComm* **2012**, *14*, 3069.